HHS Public Access

Author manuscript

J Biomech. Author manuscript; available in PMC 2018 November 07.

Published in final edited form as:

J Biomech. 2017 November 07; 64: 59–68. doi:10.1016/j.jbiomech.2017.08.031.

Computational modeling and validation of human nasal airflow under various breathing conditions

Chengyu Li[a], **Jianbo Jiang**[a,*], **Haibo Dong**[b], and **Kai Zhao**[a,†]

[a]Department of Otolaryngology-Head and Neck Surgery, The Ohio State University, Columbus, OH, USA

[b]Department of Mechanical and Aerospace Engineering, University of Virginia, Charlottesville, VA, USA

Abstract

The human nose serves vital physiological functions, including warming, filtration, humidification, and olfaction. These functions are based on transport phenomena that depend on nasal airflow patterns and turbulence. Accurate prediction of these airflow properties requires careful selection of computational fluid dynamics models and rigorous validation. The validation studies in the past have been limited by poor representations of the complex nasal geometry, lack of detailed airflow comparisons, and restricted ranges of flow rate. The objective of this study is to validate various numerical methods based on an anatomically accurate nasal model against published experimentally measured data under breathing flow rates from 180 to 1100 ml/s. The numerical results of velocity profiles and turbulence intensities were obtained using the laminar model, four widely used Reynolds-averaged Navier-Stokes (RANS) turbulence models (i.e., k- , standard k- Shear Stress Transport k- , and Reynolds Stress Model), large eddy simulation (LES) model, and direct numerical simulation (DNS). It was found that, despite certain irregularity in the flow field, the laminar model achieved good agreement with experimental results under restful breathing condition (180 ml/s) and performed better than the RANS models. As the breathing flow rate increased, the RANS models achieved more accurate predictions but still performed worse than LES and DNS. As expected, LES and DNS can provide accurate predictions of the nasal airflow under all flow conditions but have an approximately 100-fold higher computational cost. Among all the RANS models tested, the standard k- model agrees most closely with the experimental values in terms of velocity profile and turbulence intensity.

Keywords

Computational fluid dynamics (CFD); nasal airflow; medical image-based modeling

†Corresponding author: kai.zhao@osumc.edu (K. Zhao).
*Current at Voith Hydro Inc., York, PA

Conflict of interest statement

To the best of our knowledge, no conflicts of interest exist for any of the authors.

1. Introduction

The nose acts as an important component of the respiratory system with multiple vital physiological functions, including warming, filtration, humidification, and olfaction. These transport phenomena highly rely on the underlying flow physics of the nasal airflow pattern. Depending on the local Reynolds numbers (*Re*), nasal airflow patterns may undergo different flow regimes (i.e. laminar, transitional, and turbulent flows). At a moderate unilateral flow rate (e.g. 500 ml/s), the entrance flow from nares is generally considered as laminar flow, which accelerates in the nasal vestibule to become transitional flow, gradually developing into turbulent flow (Doorly et al., 2008c) due to the reduction of cross-sectional area (i.e., the nasal valve). A transition to turbulent flow usually takes place at a local *Re* of approximately 2000. Depending on the complexity of the nasal airway, the transition to turbulence may occur at a *Re* lower than this critical value. The transition to turbulent flow facilitates the exchange of heat, moisture and mass and results in better mixing, which contributes to nasal functions. For adults, unilateral flow rates can range between 80–200 ml/s for normal restful breathing and 200–1000 ml/s during sniffing and physical exercise (Anderson et al., 2006; Rennie et al., 2011), with *Re* ranging from several hundred to several thousand. Particle Image Velocimetry (PIV) measurements suggested that the unilateral flow at breathing rates less than 200 ml/s can be considered as laminar (Kelly et al., 2000; Kim and Chung, 2004). Using hot-wire anemometer probes, airflow measurements in an enlarged human nasal model (Hahn et al., 1993) also revealed airflow to be laminar in the majority of the nasal cavity at a restful breathing rate of 180 ml/s, and to be mostly turbulent under sniffing breath conditions (560 ml/s and 1100 ml/s). In contrast, dye visualization at unilateral flow rates of 115~170 ml/s (Doorly et al., 2008a) revealed flow irregularity within the nasal cavity, which make the laminar flow assumption debatable even under the restful breathing flow rate.

Compared with experimental measurements, computational fluid dynamics (CFD) simulations have unique advantage to capture nasal airflow patterns in detail. However, accurate predictions of such internal flow and turbulence features rely on the selection of appropriate CFD models. The laminar model has been commonly adopted for simulating nasal airflow at relatively low flow rates when the turbulence kinetic energy is negligible (Croce et al., 2006; Keyhani et al., 1995; Wang et al., 2016), but this approach has been questioned (Doorly et al., 2008a; Doorly et al., 2008b). To better evaluate the flow transition to turbulence, Reynolds-averaged Navier-Stokes (RANS) with two-equation turbulence models have been normally applied, such as k- model (Tan et al., 2012; Zhao et al., 2006), standard k- model (Zhang and Kleinstreuer, 2011), Shear Stress Transport (SST) k- model (Mylavarapu et al., 2009), and Reynolds Stress Model (RSM) (Ball et al., 2008). With the advancement of high performance computing, in recent years, many groups have considered large eddy simulation (LES) as an alternative approach for modeling airflow in human respiratory systems (Lu et al., 2014; Xi et al., 2016). Unlike the RANS approach, LES can directly solve the equations that describe the evolution of a large range of turbulence scales. Only the smallest scales are modeled using sub-grid-scale (SGS) models. Direct numerical simulation (DNS) does not require any turbulence models to resolve turbulent fluctuations if the time and length scales used are small enough and is often considered as the gold

standard in numerical simulations. However, the high computational cost limits its applications, and very limited studies can be found in the literature for both simplified geometries (Lin et al., 2007; Varghese et al., 2007) and human nasal cavity (Wang and Elghobashi, 2014).

The accuracy of CFD simulation heavily depends on careful selection of the modeling approach and rigorous validation. Although several validations of CFD models for human nasal airflow have been conducted, those previous studies are limited by only compare to measured global quantities, such as the total pressure drop across the nasal cavity or the static pressure on the nasal wall (Croce et al., 2006; Mylavarapu et al., 2009; Weinhold and Mlynski, 2004). A few other validation studies conducted more detailed comparisons with experimental data but with poor representation of the complex nasal geometry (Ball et al., 2008; Chen and Gutmark, 2014; Zhang and Kleinstreuer, 2011). As an exception, Doorly et al. conducted a detailed comparison between time-averaged PIV measurement and high-fidelity CFD simulation in an anatomically-accurate model of human nasal cavity at a flow rate of 150 ml/s (Doorly et al., 2008b). Still, most of these previous studies tested their CFD models on only a limited range of flow rates.

The purpose of the present study is to evaluate the accuracy of different CFD models in the prediction of detailed nasal airflow velocity and turbulence patterns under different breathing conditions within an anatomically accurate human nose. A series of simulations using the laminar model, four RANS turbulence models (k- , standard k- , SST k- , and RSM), LES and DNS are conducted in a right human nasal cavity constructed from computerized tomography (CT) scans. Detailed analysis of the velocity field and turbulence intensity at various unilateral flow rates (180, 560, and 1100 ml/s) are presented and compared with hot-wire experimental measurements of the same subject (Hahn et al., 1993).

2. Methods

2.1. Experimental setup and nasal geometry

Hahn et al. (Hahn et al., 1993) conducted experimental measurements of nasal airflow using a hot-wire anemometer in a large-scale (20×) physical model constructed based on CT scans of the right nasal cavity of a healthy male adult. In the experiments, three steady breathing flow rates equivalent to 180 ml/s, 560 ml/s, and 1100 ml/s in the real human nose were applied, corresponding to restful breathing, medium sniffing, and strong sniffing, respectively. Both velocity and turbulence intensities were measured in various sections of the nasal cavity. Fig. 1(a) shows the experimental setup and the relative position of measurement sites on the slices that were used for the current validation.

In the present study, the anatomically accurate nasal model based on the same subject (Keyhani et al., 1995) was adopted and re-meshed. The computational model included the region from the anterior tip of the nose to the posterior end of the nasal turbinate. As shown in Fig. 1(b), the nasopharynx was extended in the current CFD model to match the physical geometry in the experimental setup.

2.2. Governing equations and numerical methods

For laminar and turbulent airflow through the nose, the governing equations for the conservation of mass and momentum are given by the following:

$$\frac{\partial u_i}{\partial x_i}=0 \quad (1)$$

$$\frac{\partial u_i}{\partial t}+\frac{\partial (u_i u_j)}{\partial x_j}=-\frac{1}{\rho}\frac{\partial p}{\partial x_i}+\nu\frac{\partial}{\partial x_j}(\frac{\partial u_i}{\partial x_j}) \quad (2)$$

where $i, j = 1,2,3$; u_I are the velocity components; p is the pressure; ρ and ν are the fluid density and kinematic viscosity, respectively. Further details on the numerical methods applied in the current study can be found in the Supplemental Material.

Briefly, ANSYS Fluent 16.2 (Ansys, Inc., Canonsburg, PA, USA) was employed to implement the laminar model, four different RANS turbulence models (including k- , standard k-, SST k- , RSM), and the LES model. For the laminar and RANS simulations, second-order spatial discretization schemes were used for pressure and momentum. The SIMPLEC algorithm was used for pressure-velocity coupling. For the LES simulations, the bounded central differencing scheme was used for discretization of both the pressure and momentum equations. The PISO scheme was adopted for pressure-velocity coupling. The wall-adapted local eddy-viscosity (WALE) SGS model was employed to resolve the small eddies.

The DNS of the viscous incompressible Navier-Stokes equations was achieved using an in-house immersed-boundary-method-based solver (Dong et al., 2006; Mittal et al., 2008). The equations were solved using a fractional step method. An Adams-Bashforth scheme and an implicit Crank-Nicolson scheme were employed for the discretization of the convective terms and diffusion terms, respectively. The details of the numerical treatment and solver validations can be found in Ref. (Li and Dong, 2016, 2017; Li et al., 2015).

The computational meshes (Fig. 1(c)) for laminar, RANS and LES were generated with ICEM CFD (Ansys, Inc., Canonsburg, PA, USA). A five-layer prism mesh was adopted at the boundary with a total height of 0.2 mm near the mucosal surface to more accurately model the rapidly changing near-wall air velocity, with the first layer mesh height of 0.015 mm. Then, the initial meshes were refined by gradient adaptation and boundary adaptation until grid independence of the solutions was achieved. Since LES model generally requires the highest mesh resolution, it was selected for conducting the grid independent analysis. Grid independence analysis was conducted by investigating the pressure drop across the nasal cavity, the velocity distribution, and the turbulent intensity distribution in selected coronal sections. At a flow rate of 1100 ml/s, doubling the current mesh resulted in only 0.2% difference in the pressure drop, 0.8% difference in the maximum velocity, and 2.1% difference in the maximum turbulence intensity in the selected coronal sections. After the

grid independence analysis, the final nasal cavity mesh ranged from 2.9 million grids for the lowest flow rate simulation to 5.9 million grids for the highest flow rate simulation. For DNS simulations, a Cartesian grid was generated that range from 11.5 million for the lowest flow rate to 36.7 million for the highest flow rate. For RANS/LES mesh, the non-dimensional wall distance y^+ <1 held for all simulated domain; for DNS mesh, the grid size was predominantly finer than the Kolmogorov length scale. Further details on the validation of the grid resolution can be found in the Supplemental Material.

Both laminar and RANS simulations were performed as steady-state, matching the experimental setup. For both LES and DNS simulations which are transient in nature, the time step was specified as 1e-5 s and the number of iteration steps was 100,000, which was equivalent to 1 s and approximately 55 flow-through times of the nasal airway at 1100 ml/s, sufficient for flow to reach steady state. For steady-state solution for laminar and RANS models and LES at each time step, the convergence criteria of each variable is 1e-4. Increasing the convergence criteria to 1e-5 had been found to have a negligible effect on the simulation results (Zhang and Kleinstreuer, 2011). For all simulations, the inlet velocity boundary condition and outflow condition were used to match the experimental flow rates, and the pressure drop between inlet and outlet were obtained once a converged solution was achieved. The turbulent intensity on the inlet boundary was set as 2.2%, 2.7% and 2.5% for restfully breathing (180 ml/s), medium sniffing (560 ml/s), and strong sniffing (1100 ml/s), respectively, based on the experimental measurements of (Hahn et al., 1993).

All laminar and RANS simulations were conducted on DELL workstations with Xeon E5-2630 CPU and 64 GB of core memory. The LES simulations were conducted on the computing cluster at the Ohio Supercomputer Center (OSC) located at The Ohio State University. The DNS simulations were done on the computing cluster at the University of Virginia. In order to fairly compare the overall computational cost for all simulations, we rerun both LES and DNS simulations for several hundreds of steps on the same local workstations for estimating the total computational time, if done locally. For each simulation based on the laminar or RANS models, it took between 2 and 19 hours to reach convergence. For LES, the simulation would require anywhere from 720 to 1080 hours at equivalent local workstations. For DNS, the estimated run times ranged 1100 to 2100 hours.

3. Results

The computed velocity fields from the different numerical models were compared with experimental measurements at various matching locations for flow rates of 180 ml/s, 560 ml/s, and 1100 ml/s, corresponding to restful breathing, medium sniffing, and strong sniffing and shown in Fig. 2, Fig. 3, and Fig. 4, respectively. The velocity profiles were normalized by the maximum velocity at the naris for each flow rate. No fitting between CFD and the experimental results was performed. At the lowest flow rate (180 ml/s), the velocities have laminar-like profiles with less steep slopes near the walls (Fig. 2). As the flow rate increases to the medium (560 ml/s, Fig. 3) and high (1100ml/s, Fig. 4) values, the flow in the nasal cavity gradually transitions to turbulent, and the turbulent core makes the velocity profiles relatively flat at the cavity center and steep near the walls. As expected, the laminar model predictions are in good agreement with experimental data at the lowest flow rate (180 ml/s)

but considerably deviate from (over-estimate) the experimental values at the higher flow rates (560 ml/s and 1100 ml/s). Some of the RANS models predict better than the laminar model for the two higher flow rates with varying accuracies, but they are generally worse than LES and DNS.

The performances of the RANS models, the LES model and DNS on the prediction of turbulence intensity are shown in Fig. 5. At the flow rate of 180 ml/s, the experimentally measured turbulence intensity was less than 4% (Fig. 5(a)). For the medium and high breathing rates, moderate turbulence intensities appeared near the ceiling region ($l/L > 0.8$) of slice III, which belongs to the olfactory region (see Fig. 1(b)). The expansion of the cross-sectional area around this region might intensify the turbulence.

Most of the RANS models significantly over-predicted the turbulence intensity in the low intensity range, especially the k- and RSM models. The exception is the SST k- model, which under-predicted the turbulence intensity profiles at the low breathing rate. Compared with the RANS models, both LES and DNS achieved better agreement with the experimental data for all breathing flow rates for all turbulence intensity ranges. However, compared with DNS, the LES model slightly under-predicted the turbulence intensity at the lowest flow rate and slightly over-predicted the turbulence intensity at the medium and high flow rates.

The overall performances of the different models were evaluated by their normalized mean square error (NMSE). By definition, NMSE is defined as follows (ASTM, 2002):

$$NMSE=\frac{\overline{Q_e-Q_p}^2}{\overline{Q_e}\cdot\overline{Q_p}} \quad (3)$$

where Q represents velocity or turbulence intensity and subscripts e and p represent experimental and predicted values, respectively. The bar "-" represents an average over all the measurement points.

Comparisons of the velocity and turbulence intensity profiles were made by sampling 30 total points (locations are indicated in Fig. 1(a)) at each breathing flow rate. As suggested by ASTM (ASTM, 2002), lower NMSE values indicate better prediction by the model, and an NMSE value of 0.25 or less can be taken as generally indicative of acceptable model performance. Fig. 6 shows the NMSE values of the models used in the current study. It has been found that LES and DNS were generally more accurate than any other models at all breathing rates, except at the lowest breathing rate, where the laminar model became the best. However, the results from the laminar model were based on steady-state setup and simulated with limited mesh size, while DNS resolves the flow field at all scales. The RANS models performed better at increased breathing rates, while the reverse was true for the laminar model. The predictions of the standard k- model agreed better with the experimental data than those of the other RANS models.

Fig. 7 shows the pressure drop and local Reynolds number along the nasal airways at three different flow rates. As shown in Fig. 7, the major total pressure drop was localized within the first 1/3 of the total nasal passage (from nares to nasal valve), and the percentage of pressure drop in this region increased with increasing flow rate. Under the restful breathing condition (180 ml/s), 56.9% of the total pressure drop occurred in this region. This percentage increased to 75.3% for medium sniffing (560 ml/s) and 83.2% for strong sniffing (1100 ml/s). With the exception of k- and RSM, most numerical models achieved a good agreement with the DNS results in terms of pressure drop at all flow rates, including the laminar model at higher flow rates.

Fig. 8 compares the pressure drop between our simulation results and previous experimental measurements presented in the Table 1 of (Hahn et al., 1993). In that table, Hahn et al. compared their calculated pressure drop with the range of pressure drop measured in human subjects by (Sullivan and Chang, 1991) at the same flow rates. To make a fair comparison, we recalculated the pressure drop using the velocity gradients at central nasal cavity wall, the same way as defined in (Hahn et al., 1993). Our calculated results showed a better agreement with the human experimental measurements by (Sullivan and Chang, 1991) than (Hahn et al., 1993), especially at the highest flow rate (1100 ml/s). Compared to CFD simulation, it might be more challenging for Hahn et al. (1993) to accurately measure the slope of velocity profiles near the wall through hot-wire probes, especially at high flow rates when the near wall velocity gradient become very sharp. We suspect the underestimated velocity gradients and limited numbers of sampling points might cause the discrepancy in (Hahn et al., 1993) for the estimation of pressure drop.

Fig. 9 compares the velocity patterns and streamline patterns at different flow rates. To visualize the streamline, 100 tracking seeds were uniformly released on the nostril plane. An anterior dorsal vortex was observed at all flow rates. Both the vortex and the turbulence are likely the result of unsteadiness of the nasal airflow.

To identify the regions of the nasal cavity with strong turbulence, Fig. 10 depicts the iso-surface of time-averaged turbulence intensity at 5% and color coded by the magnitude of normalized turbulence kinetic energy. The blank nasal cavity of Fig. 10(a) indicates the flow was mostly laminar at flow rate of 180 ml/s. As the flow rate increased to 560 ml/s, significant turbulence was observed in the anterior dorsal nasal cavity and the “pharynx” channel. At the flow rate of 1100 ml/s, considerable turbulent flow was also observed around the middle and inferior turbinate regions.

4. Discussion

Human nasal airflow plays an important role in many physiological functions of the nose, such as filtering, olfaction, air-conditioning and others. In recent years, CFD has been increasingly used to predict the airflow and related transport phenomena in human nasal cavities (Bates et al., 2015; Li et al., 2017; Otto et al., 2017; Zhao and Jiang, 2014; Zhao et al., 2014a; Zhao et al., 2014b). Compared to experimental measurements, CFD has the advantages of low cost, non-invasiveness, and ease in obtaining detailed results in both the spatial and temporal domains. The selection of appropriate CFD models is critical for the

accurate prediction of human nasal airflow. The main difficulties in the choice of CFD models lie in the fact that (1) human nasal airflow is highly complicated with recirculating flow, adverse pressure gradients, airway convergence and divergence, and (2) the flow regime (laminar, transitional, or turbulent) is highly variable depending on the nasal cavity geometry and breathing conditions. Previous studies were limited either by involving only comparisons to the measured pressure drop across the nasal cavity (Croce et al., 2006; Mylavarapu et al., 2009; Weinhold and Mlynski, 2004) or over-simplified nasal geometry (Ball et al., 2008; Chen and Gutmark, 2014; Zhang and Kleinstreuer, 2011). In the current study, we validated several CFD methods in an anatomically accurate computational model by comparing simulated velocity profiles and turbulence intensities with experimental data under a greater range of breathing conditions.

It is not surprising that our comparison study showed that LES and DNS are more accurate for all given flow rates than the other models. The better performance of LES and DNS is due to their theoretical basis. The laminar model treats the airflow as an ideal laminar flow by ignoring turbulent kinetic energy. RANS models consider an integral approach for the whole turbulence spectrum, but the physics of the various scales is different. In LES, large eddies responsible for most of the mass, momentum and energy transport are explicitly resolved while the turbulent scales smaller than the grid size are filtered out and solved by SGS models. Compared to LES, DNS directly solves the N-S equations for the whole range of spatial and temporal scales without the need of any modeling. To achieve high-fidelity simulations, the DNS in the current study was conducted using a validated in-house solver (Dong et al., 2010; Koehler et al., 2011; Li and Dong, 2016; Mittal et al., 2008). The advantage of LES and DNS over other models in terms of accuracy for the analyses of various flow fields and related transport phenomena have been found in the analysis of many complex flows (Chen and Gutmark, 2014; Zhang and Kleinstreuer, 2011). However, the typical computational cost of LES or DNS is a few hundred times higher than that of other models, as presented in the current study.

The prohibitive computing resources required for DNS and LES limit their practical application for human nasal airflow. In the near future, RANS models together with the laminar model may be still the most commonly used tools due to their significantly reduced computational cost. However, the RANS models tested in the current study failed in their prediction of the laminar and transitional flow regime (Fig. 6), especially in the low flow rate case (180 ml/s). In addition, when comparing with DNS and LES, the unsatisfactory performance of these RANS models at moderate flow rate implies the inaccuracy of these models in the prediction of transitional flow behavior. Further development of more advanced RANS turbulence models is needed to improve their predicting capabilities for laminar and transitional flows in nasal airways. Overall, the standard k- model is a better choice than the other RANS models tested in this study in the prediction of human nasal airflow, as illustrated in Fig. 6. This outperformance might originate from its treatment of the viscous near-wall region and its handling of streamwise pressure gradients for wall bounded flows.

Although it is still an open question whether human nasal airflow during restful breathing (<250 ml/s) is turbulent or not, our simulations illustrated that the laminar model can achieve

good agreement with experimental data, comparable to or even better than LES and DNS results at a low flow rate of 180 ml/s. Minor irregularities and turbulence may still exist (< 5% turbulence intensity, as shown in Fig. 5(a)) at this restful breathing flow rate, yet this did not affect the accuracy of the laminar model, which may have broad applications in future investigations of respiratory airflow problems.

In addition, our study showed that global properties, such as the pressure drop across the nasal cavity or nasal resistance may not be good validation criteria. Our results showed that although the laminar model failed to capture the local velocity profiles at medium and high flow rates (Fig. 3 and Fig. 4), it still achieved reasonable agreement on the global pressure drop (Fig. 7), comparable to LES and DNS. These findings also suggest that the selection of CFD methods should also consider the study purposes. If the study goal is to estimate the global properties (such as nasal flow rate, resistance, and etc.), the laminar model could achieve reasonable results with much lower computational costs than the other models. However, if researchers are interested in other flow quantities for which the exact flow pattern are important (e.g., particle transport), then the laminar model is not suitable, and other high-fidelity models need to be considered, especially for the higher flow rates conditions.

The current study also serves as a foundation for better understanding the nasal transport phenomena (heat, mass) that are critical to the nasal functions. These transport functions depend on accurate predictions of airflow patterns and the level of turbulence. In addition to turbulence, we found an anterior airflow vortex at all nasal airflow rates (Fig. 9), which might result in further mixing and intensifying the unsteadiness of the airflow in this region. This finding demonstrated the need for accurate selection of CFD models and appropriate validation to properly investigate the nasal transport phenomena in the future.

5. Conclusions

In conclusion, we have evaluated the overall performance of seven CFD models for modeling anatomically accurate human nasal airflow with published experimental detailed velocity and turbulence profiles as benchmarks. LES and DNS were the most accurate at all flow rates but required much greater computational resources. The laminar model predictions matched well to the experimental data for restful breathing, comparable to LES and DNS. Among the four RANS models, the standard k- model gave the best overall performance during strong and moderate sniffing in terms of accuracy and computational cost.

Supplementary Material

Refer to Web version on PubMed Central for supplementary material.

Acknowledgments

This research was supported by NIH NIDCD R01 DC013626 to KZ and NSF CBET 1605232 to HD. The authors would like to thank Dr. Peter W. Scherer, University of Pennsylvania, for sharing their experimental results.

References

Anderson NJ, Cassidy PE, Janssen LL, Dengel DR. Peak inspiratory flows of adults exercising at light, moderate and heavy work loads. JOURNAL-INTERNATIONAL SOCIETY FOR RESPIRATORY PROTECTION. 2006; 23:53.

ASTM. Annual Book of American Society for Testing Materials Standards. American Society for Testing Materials; West Conshohocken, PA: 2002. Standard guide for statistical evaluation of indoor air quality models (D5157-97).

Ball C, Uddin M, Pollard A. High resolution turbulence modelling of airflow in an idealised human extra-thoracic airway. Comput Fluids. 2008; 37:943–964.

Bates AJ, Doorly DJ, Cetto R, Calmet H, Gambaruto A, Tolley N, Houzeaux G, Schroter R. Dynamics of airflow in a short inhalation. J R Soc Interface. 2015; 12:20140880. [PubMed: 25551147]

Chen J, Gutmark E. Numerical investigation of airflow in an idealized human extra-thoracic airway: a comparison study. Biomechanics and modeling in mechanobiology. 2014; 13:205–214. [PubMed: 23619907]

Croce C, Fodil R, Durand M, Sbirlea-Apiou G, Caillibotte G, Papon JF, Blondeau JR, Coste A, Isabey D, Louis B. In vitro experiments and numerical simulations of airflow in realistic nasal airway geometry. Annals of biomedical engineering. 2006; 34:997–1007. [PubMed: 16783655]

Dong H, Mittal R, Bozkurttas M, Lauder GV, Madden P. Computational Modeling and Analysis of the Hydrodynamics of a Highly Deformable Fish Pectoral Fin. J Fluid Mech. 2010

Dong H, Mittal R, Najjar FM. Wake topology and hydrodynamic performance of low-aspect-ratio flapping foils. J Fluid Mech. 2006; 566:309–343.

Doorly D, Taylor D, Franke P, Schroter R. Experimental investigation of nasal airflow. Proceedings of the Institution of Mechanical Engineers, Part H: Journal of Engineering in Medicine. 2008a; 222:439–453.

Doorly D, Taylor D, Gambaruto A, Schroter R, Tolley N. Nasal architecture: form and flow. Philosophical Transactions of the Royal Society of London A: Mathematical, Physical and Engineering Sciences. 2008b; 366:3225–3246.

Doorly D, Taylor D, Schroter R. Mechanics of airflow in the human nasal airways. Respiratory physiology & neurobiology. 2008c; 163:100–110. [PubMed: 18786659]

Hahn I, Scherer PW, Mozell MM. Velocity profiles measured for airflow through a large-scale model of the human nasal cavity. Journal of Applied Physiology. 1993; 75:2273–2287. [PubMed: 8307887]

Kelly J, Prasad A, Wexler AS. Detailed flow patterns in the nasal cavity. Journal of Applied Physiology. 2000; 89:323–337. [PubMed: 10904068]

Keyhani K, Scherer P, Mozell M. Numerical simulation of airflow in the human nasal cavity. Journal of Biomechanical Engineering. 1995; 117:429–441. [PubMed: 8748525]

Kim S, Chung S. An investigation on airflow in disordered nasal cavity and its corrected models by tomographic PIV. Measurement Science and Technology. 2004; 15:1090.

Koehler C, Wischgoll T, Dong H, Gaston Z. Vortex Visualization in Ultra Low Reynolds Number Insect Flight. IEEE Trans Vis Comput Graphics. 2011; 17:2071–2079.

Li C, Dong H. Three-dimensional wake topology and propulsive performance of low-aspect-ratio pitching-rolling plates. Phys Fluids. 2016; 28:071901.

Li C, Dong H. Wing kinematics measurement and aerodynamics of a dragonfly in turning flight. Bioinspir Biomim. 2017; 12:026001. [PubMed: 28059781]

Li C, Dong H, Liu G. Effects of a dynamic trailing-edge flap on the aerodynamic performance and flow structures in hovering flight. J Fluids Struct. 2015; 58:49–65.

Li C, Farag AA, Leach J, Deshpande B, Jacobowitz A, Kim K, Otto BA, Zhao K. Computational fluid dynamics and trigeminal sensory examinations of empty nose syndrome patients. The Laryngoscope. 2017; 127:E176–E184. [PubMed: 28278356]

Lin CL, Tawhai MH, McLennan G, Hoffman EA. Characteristics of the turbulent laryngeal jet and its effect on airflow in the human intra-thoracic airways. Respiratory physiology & neurobiology. 2007; 157:295–309. [PubMed: 17360247]

Lu M, Liu Y, Ye J, Luo H. Large Eddy simulation of flow in realistic human upper airways with obstructive sleep. Procedia Computer Science. 2014; 29:557–564.

Mittal R, Dong H, Bozkurttas M, Najjar FM, Vargas A, von Loebbecke A. A versatile sharp interface immersed boundary method for incompressible flows with complex boundaries. J Comput Phys. 2008; 227:4825–4852. [PubMed: 20216919]

Mylavarapu G, Murugappan S, Mihaescu M, Kalra M, Khosla S, Gutmark E. Validation of computational fluid dynamics methodology used for human upper airway flow simulations. Journal of biomechanics. 2009; 42:1553–1559. [PubMed: 19501360]

Otto BA, Li C, Farag AA, Bush B, Krebs JP, Hutcheson RD, Kim K, Deshpande B, Zhao K. Computational fluid dynamics evaluation of posterior septectomy as a viable treatment option for large septal perforations. International Forum of Allergy & Rhinology. 2017; 7:718–725. [PubMed: 28544511]

Rennie CE, Gouder KA, Taylor DJ, Tolley NS, Schroter RC, Doorly DJ. Nasal inspiratory flow: at rest and sniffing. International forum of allergy & rhinology. 2011; 1:128–135. [PubMed: 22287331]

Sullivan KJ, Chang H. Steady and oscillatory transnasal pressure-flow relationships in healthy adults. Journal of Applied Physiology. 1991; 71:983–992. [PubMed: 1757337]

Tan J, Han D, Wang J, Liu T, Wang T, Zang H, Li Y, Wang X. Numerical simulation of normal nasal cavity airflow in Chinese adult: a computational flow dynamics model. European Archives of Oto-Rhino-Laryngology. 2012; 269:881–889. [PubMed: 21938528]

Varghese SS, Frankel SH, Fischer PF. Direct numerical simulation of stenotic flows. Part 1. Steady flow. J Fluid Mech. 2007; 582:253–280.

Wang T, Chen D, Wang P, Chen J, Deng J. Investigation on the nasal airflow characteristics of anterior nasal cavity stenosis. Brazilian Journal of Medical and Biological Research. 2016:49.

Wang Y, Elghobashi S. On locating the obstruction in the upper airway via numerical simulation. Respiratory physiology & neurobiology. 2014; 193:1–10. [PubMed: 24389271]

Weinhold I, Mlynski G. Numerical simulation of airflow in the human nose. European Archives of Oto-Rhino-Laryngology and Head & Neck. 2004; 261:452–455.

Xi J, Kim J, Si XA. Effects of nostril orientation on airflow dynamics, heat exchange, and particle depositions in human noses. European Journal of Mechanics-B/Fluids. 2016; 55:215–228.

Zhang Z, Kleinstreuer C. Laminar -to-turbulent fluid–nanoparticle dynamics simulations: model comparisons and nanoparticle-deposition applications. International Journal for Numerical Methods in Biomedical Engineering. 2011; 27:1930–1950.

Zhao K, Dalton P, Yang GC, Scherer PW. Numerical modeling of turbulent and laminar airflow and odorant transport during sniffing in the human and rat nose. Chemical senses. 2006; 31:107–118. [PubMed: 16354744]

Zhao K, Jiang J. What is normal nasal airflow? A computational study of 22 healthy adults. International forum of allergy & rhinology. 2014; 4:435–446. [PubMed: 24664528]

Zhao K, Jiang J, Pribitkin EA, Dalton P, Rosen D, Lyman B, Yee KK, Rawson NE, Cowart BJ. Conductive olfactory losses in chronic rhinosinusitis? A computational fluid dynamics study of 29 patients. International forum of allergy & rhinology. 2014a; 4:298–308. [PubMed: 24449655]

Zhao K, Malhotra P, Rosen D, Dalton P, Pribitkin EA. Computational fluid dynamics as surgical planning tool: a pilot study on middle turbinate resection. The Anatomical Record. 2014b; 297:2187–2195. [PubMed: 25312372]

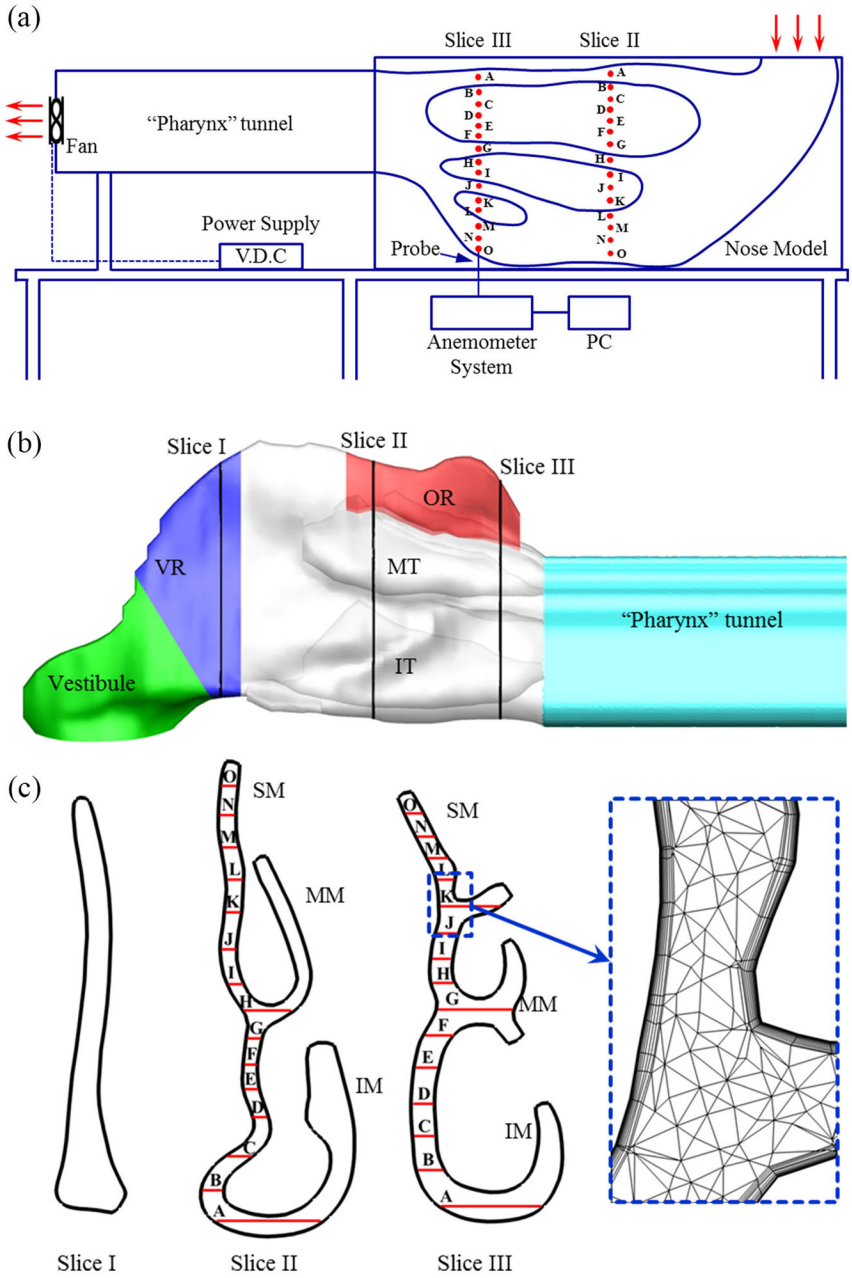

Fig. 1.

(a) A schematic diagram of the experimental apparatus. The measurement holes used in the current study are indicated by red dots on the model. The plot is reproduced base on Ref. (Hahn et al., 1993). (b) Computational model of the right human nasal cavity based on the same CT-scan as the experimental setup. The surface geometry included four functional sections: vestibule, valve region (VR), turbinate region (including inferior turbinate (IT) and middle turbinate (MT)), and olfactory region (OR). The airways between the turbinates were termed: inferior meatus (IM), middle meatus (MM), and superior meatus (SM), respectively. The posterior end of the original model was extended to match the experimental setup. (c) Coronal cross-sections at different locations along the right nasal airway. Total 30 sampling

locations on slice II and III are used to compare with experimental measurements. To capture the rapid near wall changes of air velocity, body-fitted multilayer mesh was adopted and shown in a close-up view.

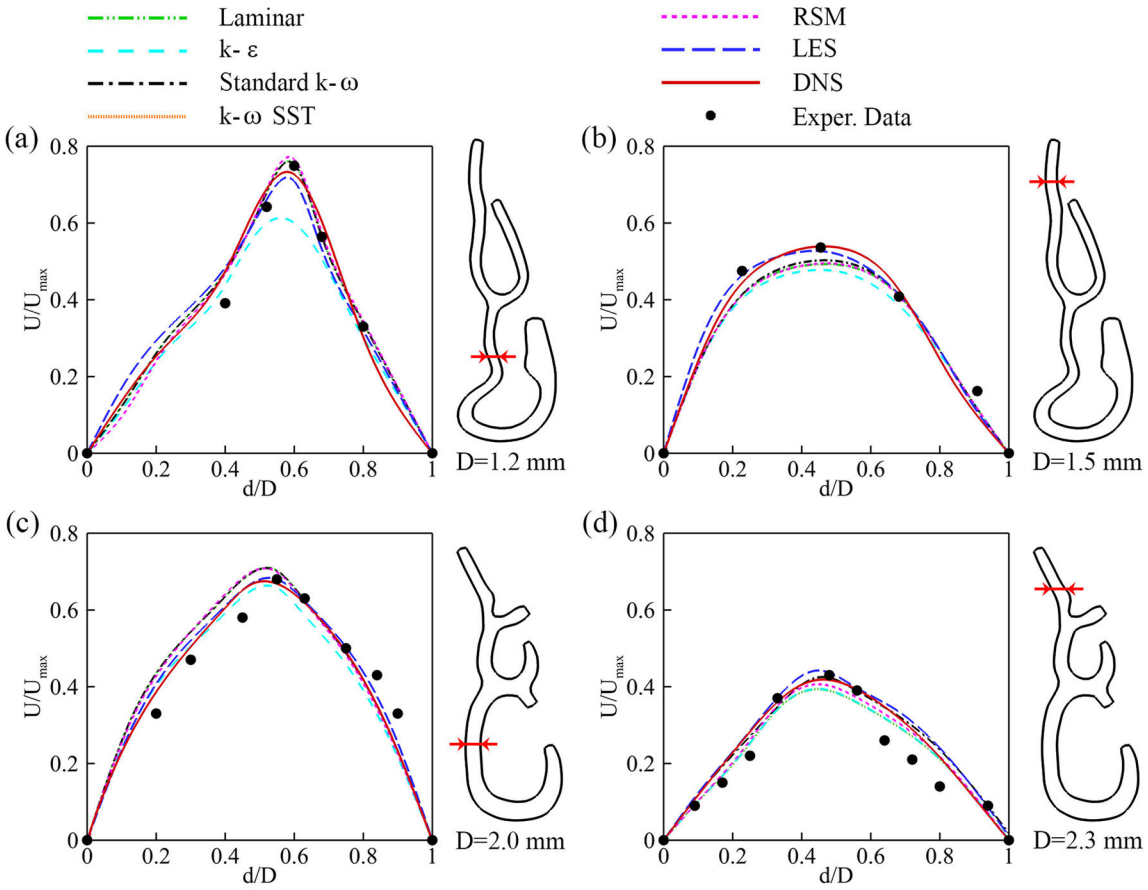

Fig. 2.

Comparison of normalized cross-sectional velocity profiles at slices II (a–b) and III (c–d) with experimental measurements (Hahn et al., 1993) at flow rate of 180 ml/s. The locations of the comparisons across the airway are indicated on the planes next to each plot.

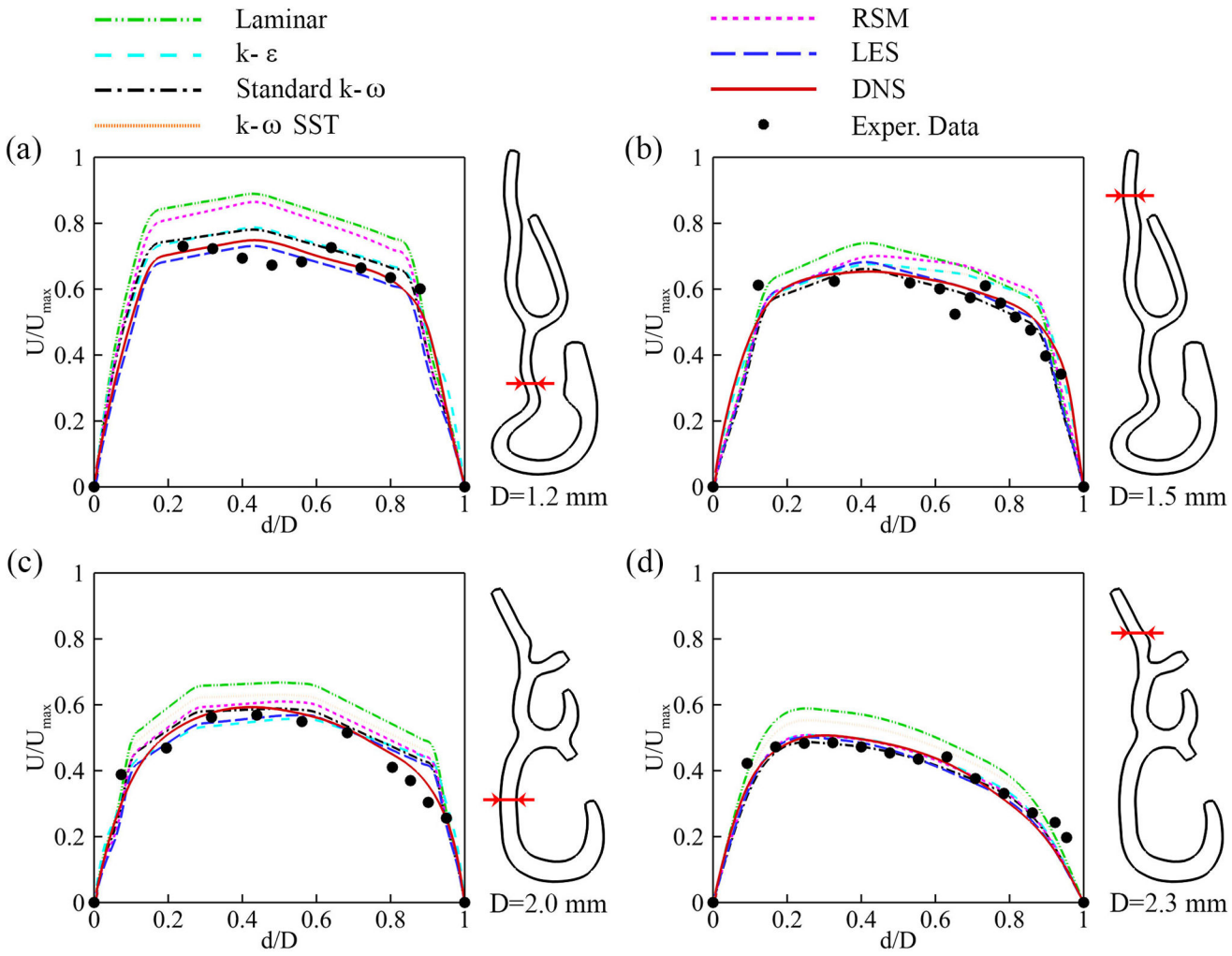

Fig. 3.

Comparison of normalized cross-sectional velocity profiles at slices II (a–b) and III (c–d) with experimental measurements (Hahn et al., 1993) at flow rate of 560 ml/s. The locations of the comparisons across the airway are indicated on the planes next to each plot.

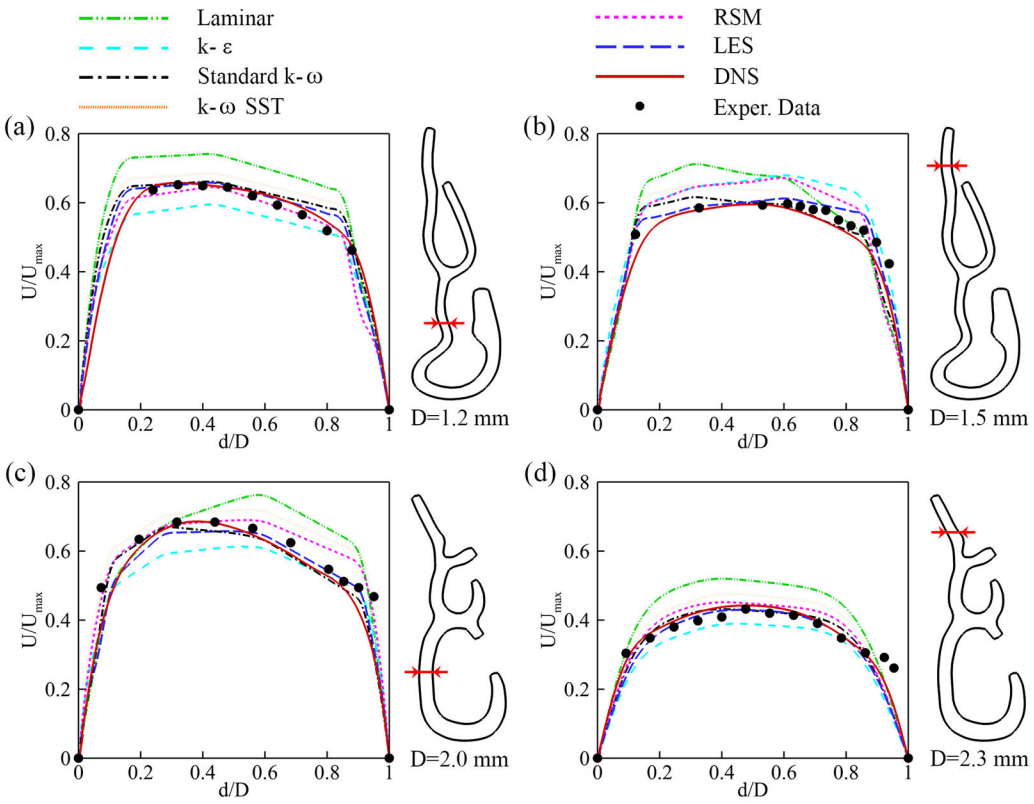

Fig. 4.

Comparison of normalized cross-sectional velocity profiles at slices II (a–b) and III (c–d) with experimental measurements (Hahn et al., 1993) at flow rate of 1100 ml/s. The locations of the comparisons across the airway are indicated on the planes next to each plot.

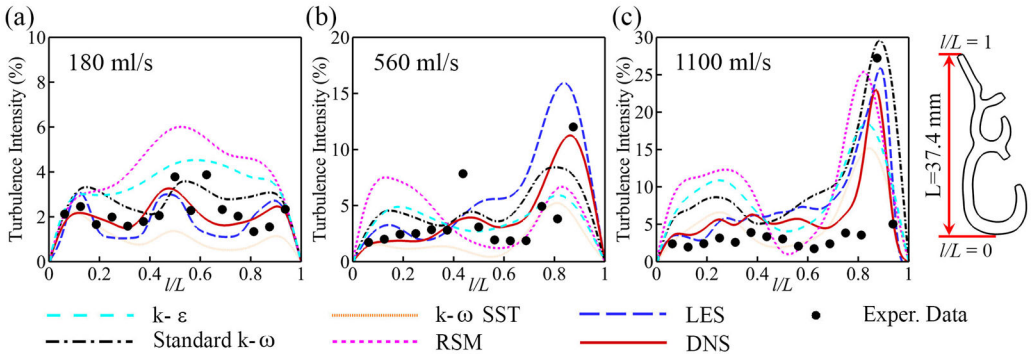

Fig. 5.

Comparison of turbulence intensity along slice III with experimental measurements (Hahn et al., 1993) at various flow rates 180 ml/s (a), 560 ml/s (b), and 1100 ml/s (c), respectively.

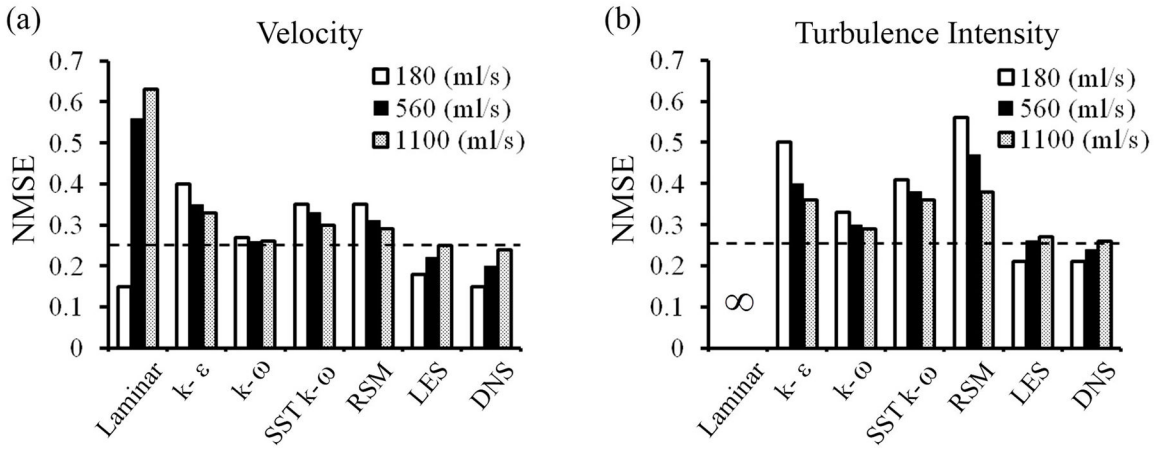

Fig. 6.

Normalized mean square error (NMSE) for the velocity profiles (a) and the turbulence intensities (b) with respect to the experimental measurements (Hahn et al., 1993). The dashed line indicates the NMSE value of 0.25. An NMSE value of 0.25 or less can be taken as generally indicative of acceptable model performance (ASTM, 2002).

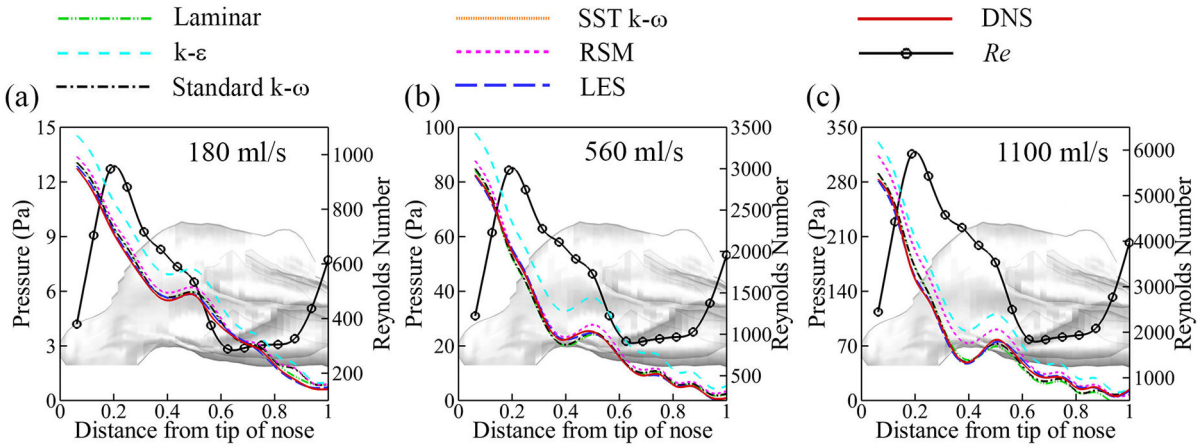

Fig. 7.

Comparison of cross-sectional pressure drop and Reynolds number (*Re*) as a function of distance to the nostril at flow rates of (a)180 ml/s, (b)560 ml/s, (c)1100 ml/s. The *Re* is calculated based on the DNS results.

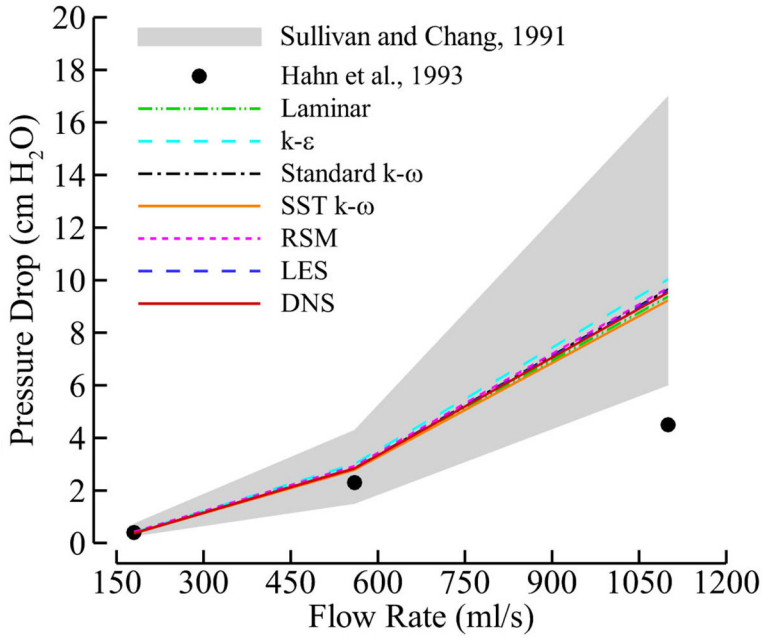

Fig. 8.

Comparison of pressure drop between current numerical simulations and previous experimental measurements at various flow rates. The gray shaded area represents the range of measured pressure drop by (Sullivan and Chang, 1991) in human subjects. The black dots indicate the experimental measurements in nasal cavity model (Hahn et al., 1993).

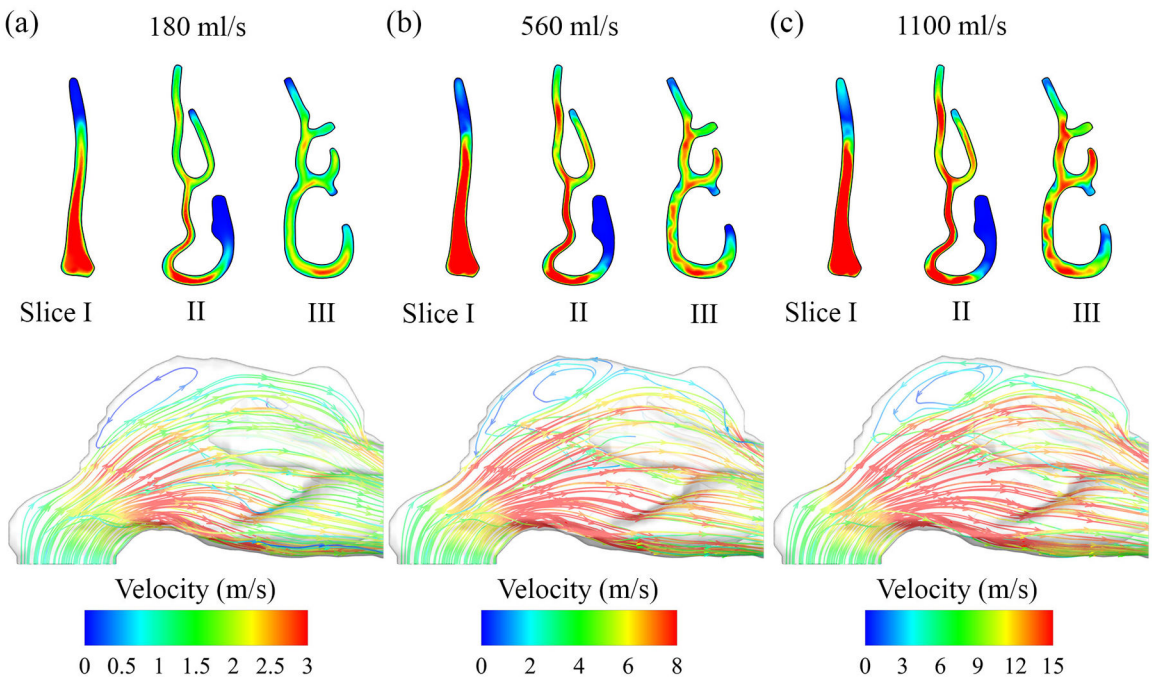

Fig. 9.

Cross-sectional velocity contours and streamline patters of the nasal airflow at flow rates of 180 ml/s (a), 560 ml/s (b), 1100 ml/s (c). The results were obtained with DNS.

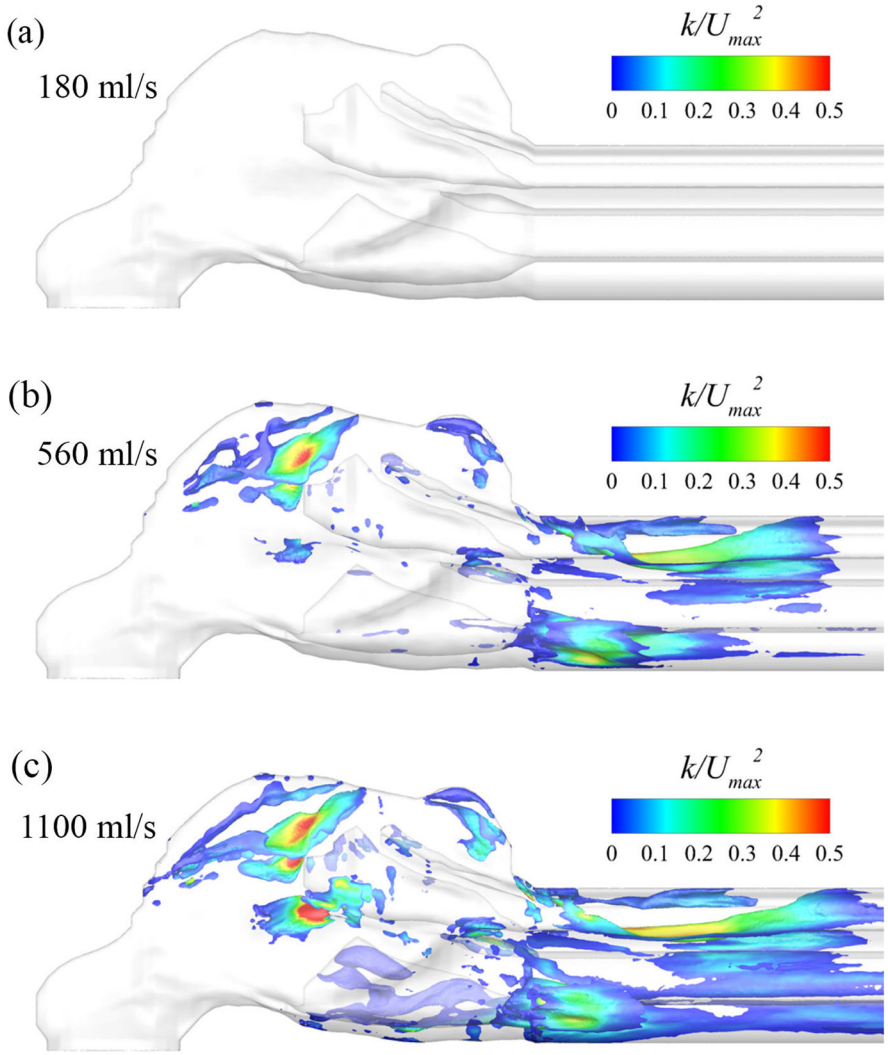

Fig. 10.

Iso-surface of time-averaged turbulence intensity at a value of 5%. The iso-surface is color coded by the magnitude of normalized turbulence kinetic energy. (a) 180 ml/s. (b) 560 ml/s. (c) 1100 ml/s. The results were obtained with DNS.